Revision 2

Geochemical processes and mechanisms for Cs enrichment in a hot-spring system

Wei Wang[a], Shao-Yong Jiang [a*], Hai-Zhen Wei [b]

[a] *State Key Laboratory of Geological Processes and Mineral Resources, Collaborative Innovation Center for Exploration of Strategic Mineral Resources, China University of Geosciences, Wuhan 430074, PR China*

[b] *State Key Laboratory for Mineral Deposits Research, School of Earth Sciences and Engineering, Nanjing University, Nanjing 210023, PR China*

*Corresponding author: shyjiang@cug.edu.cn

ABSTRACT:

Geothermal systems in Tibet, a crucial geothermal region in China, belong to the Mediterranean–Himalayan geothermal belt and are characterized by a broad distribution of Cs-bearing geyserite deposits. Targejia, one of the largest Cs-bearing geyserites in southern–western Tibet, contains 1.446×10^4 tons of Cs. The highest ore grade reaches 2.89 wt.%, and the ore-forming process can be subdivided into mineralization stages I to V. Cs is heterogeneously distributed in geyserites. Herein, two Cs-bearing ores are investigated, with distinct characteristics of (1) low Cs-bearing ore (amorphous silica opal-A and opal-CT type) with low Cs (average of ~0.2 wt.%), Na, K, Al, and Ca contents, and (2) high Cs-bearing ore (clay type) with high

Cs (average of ~1.40 wt.%), Na, K, Al, and Ca contents. It is reported for the first time that Cs primarily exists in clay rather than in amorphous silica opal. The Cs-enrichment mechanisms are different for the above two Cs-bearing geyserite types. (1) The deprotonated –OH, surrounded by water molecules, controls the amount of Cs absorbed on the geyserite surface (Si–OH) in the low Cs-bearing ore. (2) The variable Cs content depends on the Al content because Al substitutes Si, yielding more negative charges to absorb Cs in the high Cs-bearing ore. Geothermal fluid loading-mass elements, such as Cs and SiO_2, precipitate as amorphous silica (opal) with clay minerals. Mineral saturation index modeling was used to predict the most applicable physical parameters for ore formation. The results confirm that the ore forms at ~85 °C and a pH of ~8.5 in the Na–Cl system at stage V. The degree of Cs enrichment reduces from the latest stage V (0–4 ka) to the early stage IV (4–17 ka), and is controlled by clay dissolution, which might further relate to the climate change in Tibet's Holocene. Fluid–rock interaction modeling shows that dissolution–reprecipitation induces a higher order of amorphous silica formation and clay dissolution at >40 °C and pH of 5–9 at stages V and III, excluding Cs from the ore.

Keywords: Cs, enrichment mechanism, amorphous silica, clay

1. Introduction

Owing to its excellent optoelectronic properties and strong chemical activity, Cesium (Cs) is a critical metal widely used in vacuum device and phototube manufacturing. So far, Cs deposits can be divided into granite–pegmatite (Černý, 1978) and hot-spring types (Guo et al., 2008). Hot-spring deposits closely relate to geothermal systems because sinter deposits precipitated from geothermal fluids contain many ore elements (i.e., Au, Ag, Li, B, As, Mo, Hg, Cu, Pb, Sb, and W) (Fig. 1a) (Rui and Shen, 1992; Lynne et al., 2007). Sinters represent a rare situation among low epithermal hydrothermal systems because metal mineralization occurs in subaerial siliceous sinters (Lynne et al., 2007).

The Yunnan–Tibet geothermal belt (YTGB), part of the Himalayan geothermal belt, is in the primary collision zone with intense tectonic deformation between the Indian and Eurasian plates, where intense modern geothermal activities are developed (T'ung et al., 1981). Geothermal systems, including geothermal fluids and their sediments, have been used as tracers for recording the changes in external surroundings and climate and reflecting the tectonic–thermal events in the plateau's rapid uplifting process in recent several million years or several hundred-thousand years (Hou et al., 2001). Along the YTGB, large-scale silica sinters (opal-A, opal-CT, and opal-C) form as discharging thermal fluids cool at the surface below 100°C (Guidry and Chafetz, 2002).

In Tibet, China, a new type of Cs-bearing geyserite was found in 1986.

This is the peer-reviewed, final accepted version for American Mineralogist, published by the Mineralogical Society of America.
The published version is subject to change. Cite as Authors (Year) Title. American Mineralogist, in press.
DOI: https://doi.org/10.2138/am-2022-8532. http://www.minsocam.org/

Geothermal fluids have high Cs contents (up to ~50 μg/mL), and parts of Cs-bearing geyserites constitute large-scale Cs deposits (Zheng et al., 1995). The Targejia hot-spring Cs deposit is one of the largest Cs deposits in Tibet and represents the focus of an ongoing exploration program for high-grade Cs ore (Zheng et al., 1995; Zhao et al., 2006a, b, 2008). The Cs potential resources in the area yield 1.446×10^4 t (ore grade up to 1.55 wt.%) (Zheng et al., 1995).

The Cs enrichment in geothermal fluids can be attributed to the partial melting of the Qinghai–Tibet Plateau's crust, magma evolution, and fluid–rock interaction (Li et al., 2006). The collision between India and Asia is one crucial factor in partial melting (Li et al., 2006). When geothermal fluids loading high Cs, H_4SiO_4, Na, B, and Li contents ascend to the surface, minerals (primarily amorphous silica) with these elements form along with various physical and chemical parameters, such as CO_2 degassing, temperature, and pressure decrease (Zhao et al., 2006b). Cs occurs as three distinctive ore types: opal-A, opal-CT, and opal-C.

Typically, the phase transformation scenario is that amorphous opal-A precipitates first, and a diagenetic process promotes opal-A transformation into paracrystalline opal-CT and/or well-ordered opal-C, and finally into more stable and microcrystalline quartz (Lynne, 2015). The phase transformation scenario and most studies have shown that the mineralized opal-A alternates to barren opal-C based on whole-rock data, indicating that precious metal Cs deposition was modified (Zheng et al., 1995; Zhao et al., 2006a, b). Cs is in the Q^2 and Q^3 constructs of amorphous silica.

The Q^2 site, $Si(OSi)_2(OH)_2$, refers to a Si atom linked to two other Si atoms through two bridging oxygen atoms, whereas the Q^3 site, $Si(OSi)_3(OH)$, refers to a Si atom linked to three other Si atoms (Luo et al., 2012; Zhou et al., 2013).

The progressive dehydration and polymerization of amorphous silica (loss of H_2O, Si–OH + HO–Si = Si-O–Si + H_2O) explain the reduced degree of Cs enrichment and phase transformation because Cs primarily exists as OCs^- by substituting −OH in amorphous silica (Si–OH) (Zheng 1995; Zhao et al. 2006b, 2008, 2010). However, for most epithermal deposits, such as Au at the McLaughlin Mine hot-spring gold deposit and the low-sulfidation epithermal deposits of the Omu Camp in Hokkaido, Japan, the Au distribution is heterogeneous in ore and controlled by different formation mechanisms (Sherlock and Lehrman, 1995, 2005; Zeeck et al., 2021). Research on Cs ore whole-rock is limited and more studies are needed to reveal the detailed ore-forming process and the enrichment mechanisms in this type of Cs deposit.

This study investigated high-grade Cs ore (clay) and low-grade Cs ore (opal) in the Targejia deposit using in situ analysis. To investigate in detail the geothermal fluid mineralization process, including Cs migration–precipitation–enrichment–dissolution processes from deep to shallow, the mineralogical and geochemical characteristics were determined using X-ray diffraction (XRD), X-ray fluorescence spectroscopy (XRF), inductively coupled plasma (ICP) mass spectrometry (MS), in situ scanning electron microscopy (SEM) energy-dispersive spectrometry (EDS), transmission electron microscopy (TEM), in situ electron microprobe (EMPA), and

laser ablation (LA) multicollector (MC) ICP-MS. Furthermore, an essential part of this study is simulating the geothermal fluid mineralization process using the mineral saturation index model and the fluid–rock interaction model by the PHREEQC code.

2. Geological Background

The Tibetan–Himalayan orogen, the largest mountain chain on Earth today, resulted from the continued convergence between the Indian and Eurasian continents (Li et al., 2015 and reference in). The electron-spin resonance dating data of geothermal sediments in the Tibetan Plateau show an uplifting history of the plateau since 0.5 Ma B.P. in the Pleistocene (Li et al., 2001), where the climate changes from severely cold and semi-arid to arid (Han et al., 2009). Targejia's mean annual rainfall and evaporation rates are ~192 mm/yr. and ~2269 mm/yr., respectively. The mean annual temperature is approximately 0.4 °C and ranges from −13.4 °C in January to 11.7 °C in July (Zheng et al., 1995).

In Tibet, a N–S rift controls the hot-spring Cs deposits (Hou et al., 2001; Li et al., 2005). The compression of the Indian and Eurasian plates caused this rift system (Zhao et al., 2010). The Targejia deposit is close to the Yarlung Zangbo suture zone, with an average of more than 5000 m above sea level (Fig. 1b), and is covered by unconsolidated Quaternary sediments (loess) and siliciclastic sedimentary rocks (conglomerate and sandstone) from Tertiary to Jurassic (Fig. 1c). The Targejia deposit is to the south of the intersection of three fault sets (NNE, NNW, and NW) (Fig. 1c),

the Sangsang District, Anren County, Xigaze region, southern–western Tibet, China (Zhao et al., 2008). Five mineralization stages (I to V) have been classified from top to bottom of the terraces based on field observations, petrographic features, and mineralogy (Fig. 1d, e) (Zheng et al. 1995; Zhao et al. 2006a, 2008). (1) Stage I is 255 ± 63/−41.5 to 201 ± 36 ka B.P., (2) stage II is 99 ± 12.3 ka B.P., (3) stage III is 39.4 ± 1.9 to 25.0 ± 3.9 ka B.P., (4) stage IV is 14.8 ± 2.5 to 4.4 ± 3.4 ka B.P., and (5) stage V is modern (Zhao et al. 2006a). The mineral assemblage is primarily opal-CT in stages I, II, III, and IV and opal-A in stage V. Unit I comprises calc sinter (36.7 ± 3.7 to 39.6 ± 2.7 ka B.P.).

Intensive geothermal activities or ore-forming fluids are observed in the field, including hydrothermal outbreaks, high-temperature boiling springs, and cold springs (Zhong et al., 1996). The mineralization of stage V is closely associated with the primary geothermal vent of ~4 m diameter (Fig. 1d), and the primary geothermal vent fluids' Cs concentrations are up to ~5 μg/mL (Zheng et al., 1995; Wang et al., 2019). Large silica sinters (up to 16 m thick), incorporating high Cs contents (up to 1.55 wt.%), spread over the terrace at stage V (Zheng et al., 1995). The ore grade shows a wide variation from 0.2 wt.% to 1.55 wt.% (Zheng et al., 1995; Zhao et al., 2008).

3. Sampling and Analytical Methods

Samples from Targejia were collected from unit I, mineralization stages I, II, IV, and V (Fig. 1d). Table A1 lists the mineralogy and major element whole-rock

compositions. Whole-rock (Table A1) and in situ microarea analyses (Table A2, A3) were conducted on all samples, including major and trace element concentrations.

3.1 Mineralogical characteristics

The mineralogy of the samples was studied using XRD (Bede-D1) with CuKα radiation (X′TRA) and SEM. The XRD samples were dried and ground to a grain size of ~75 μm by agate. The analyses were performed in a 2θ range between 3° and 51° using a step of 0.02° and a collection time of 0.24 s/step. The polished carbon-coated thin sections were examined using a JEOL JCM-7000 SEM, fitted with an EDS system at the Collaborative Innovation Center for Exploration of Strategic Mineral Resources, China University of Geosciences (Wuhan). Imaging was performed at a working distance of 10 mm and an accelerating voltage of 15 kV. The microstructural analyses of the samples were conducted on a Thermo Fisher TEM Talos F200 X, with a field emission gun as the electron source operating at 200 kV accelerating voltages. The samples were examined after 30 min of reaction time.

3.2 Major and trace elements analysis

For major element analysis, samples mixed with 0.9 g $Li_2B_4O_7$–$LiBO_2$ flux were digested at 1050–1100 °C. After melting, the samples were measured using XRF with an AXIOS Mineral Spectrometer, with an analytical relative standard deviation (RSD) of <±0.1%–5.0%. For trace element analysis, approximately 50 mg of powdered

167 samples were digested using HF–HNO_3 at 160 °C. Trace elements were determined
168 using ICP-MS, with an analytical RSD of <±5%.

169 The in situ distribution of elements in solid samples (the same polished thin
170 sections for SEM) was determined using a JEOL JXA-8230 electron probe
171 microanalyzer (EPMA) equipped with five wavelength-dispersive spectrometers
172 (WDSs) at the Laboratory of Microscopy and Microanalysis, Wuhan Microbeam
173 Analysis Technology Co. Ltd and LA-ICP-MS at the Geological Processes and
174 Mineral Resources, China University of Geosciences, Wuhan. The EPMA samples
175 were coated with a thin conductive carbon film before analysis. Details of EPMA
176 methods have been described by Zhang and Yang (2016) and Yang et al. (2022).

177 The operating conditions for quantitative WDS analyses involved an accelerating
178 voltage of 15 kV, beam current of 20 nA, and 20-μm spot size to avoid time-
179 dependent intensity variations. Data were corrected online using an atomic number,
180 absorption, fluorescence (ZAF) correction procedure. The H_2O content was calculated
181 based on the difference to reach the analytical total of 100 wt.% and incorporated into
182 the ZAF correction procedure. The peak counting time was 10 s for K, Ca, Mg, Al, Fe,
183 Na, Si, and Cs and 20 s for Ti. The background counting time was half of the peak
184 counting time on the high- and low-energy background positions. The following
185 standards were used: microcline (K), diopside (Ca, Mg), pyrope garnet (Al, Fe),
186 jadeite (Na), olivine (Si), pollucite (Cs), and rutile (Ti). The detection limits (3σ) for
187 K, Ti, Ca, Mg, Al, Na, Si, Cs, and Fe were 147 μg/mg, 219 μg/mg, 201 μg/mg, 174

188 μg/mg, 243 μg/mg, 369 μg/mg, 531 μg/mg, 729 μg/mg, and 351μg/mg, respectively.

189 For LA-ICP-MS, in situ trace element analyses were performed on polished thin
190 sections using RESOlution S-155 LA system coupled to a Thermo iCAP Qc ICP-MS.
191 Helium was used as the carrier gas and argon as the compensation gas. The NIST
192 SRM 612 and 610 glass standards and the USGS reference glasses (BIR-1G, BCR-
193 2G, and BHVO-2G) were repeatedly analyzed between samples. Both standards and
194 samples were ablated using a 33 μm spot size, 10 Hz repetition rate, 40 s counting
195 time, and a corresponding energy density of ~3 J/cm^2.

196

197 # 4. Results

198 ## 4.1 Major elements and Cs concentration of whole-rock

199 The contents of the primary whole-rock components, SiO_2, Al_2O_3, Na_2O, CaO,
200 and K_2O, were 87.6 wt.% to 94.8 wt.%, 0.3 to 5.7 wt.%, 0 to 0.7 wt.%, 0.5 to 0.7
201 wt.%, and 0.3 to 1.0 wt.%, respectively (Table A1). Cs contents significantly vary
202 from 2034 to 9030 μg/mg (Table A1). Compared to amorphous phases, Cs contents in
203 high crystalline minerals, quartz, and calcite are low (0–600 μg/mg) (Table A1).
204 Sample DGJ-10A was collected close to the primary spring vent where geothermal
205 fluids contain high Cs contents (~5 μg/mL) at stage V and especially incorporates the
206 highest Cs grade (~9000 μg/mg). However, other amorphous opal samples are
207 characterized by low grades (~2000 μg/mg) (Table A1). These results correlate well
208 with earlier studies (Table A1) (Zheng et al., 1995; Li, 2002; Zhao et al., 2008).

209

210 4.2 Mineralogy and microtextures of Cs ore

211 The samples' mineral phases were identified using an optical microscope, SEM,
212 and XRD. At stage V, samples DGJ-9A and DGJ-10A display significantly different
213 mineral compositions than other samples, as they primarily comprise amorphous opal-
214 A. Furthermore, illite was identified using elemental and XRD analyses (Fig. A1a,
215 Fig. A2). Samples DGJ-6, 8, and 11 from stages IV and V primarily comprise opal-
216 CT (Fig. A1b). In stages I and II, DGJ-16 and DGJ-18 are the oldest samples,
217 comprising quartz crystals and other minerals, such as kaolinite, amorphous opal,
218 microcline, and calcite (Table A1). These results are consistent with the mineralogical
219 assemblages of the study area described previously (Zhao et al., 2006b, 2008).

220 At the microscale, three distinct textures of Cs-bearing geyserite were observed
221 (M1, M2, and M3). (1) M1 is granular opal with no significant color (Fig. 2a) and
222 element variation (Fig. 2, Fig. 3) in opal-CT and opal-A, and this type is the most
223 common in the ore. (2) M2 comprises alternating, irregular concentric bands or shells
224 of color, and this type only occurs in opal-A (Fig. 2b–2c, 2f–2g). As the color
225 changes, the mineral compositions (amorphous silica vs. clay) associated with
226 elemental compositions change accordingly (Fig. 4) (Section 4.3). (3) M3 is quartz
227 cemented by amorphous opal (Fig. 2d, 2h). This is the first time reporting that distinct
228 structures and clay minerals coexist on a microscale in Cs-bearing ore.

229 In summary, opal-A formed at stage V incorporates two constructs (M1 and M2),

whereas opal-CT formed at stages IV and V comprises only M1. M3 type was observed in sample DGJ-16 with the oldest age.

4.3 In situ major and trace elemental compositions in M1, M2, and M3

The major elements of the three constructs in opal-A, opal-CT, and quartz are analyzed using in situ EPMA, and the trace elements of M2 in opal-A are analyzed using LA-ICP-MS. Na, Al, K, Si, Ca, Cs, and H_2O are the primary components, accounting for more than 99.9% of the samples (Table A2). Furthermore, rare metals (Li, 0–44 μg/mg; Be, 0.6–600 μg/mg; B, 0–400 μg/mg; Ga, 0–585 μg/mg; Rb, 20–300 μg/mg; Sr, 0–625 μg/mg) were obtained (Table A3).

Type M1: Cs is evenly distributed in amorphous opal-CT at stages V and IV (Fig. 3). This amorphous silica incorporates low contents of Cs_2O (0.06–0.36 wt.%, av. 0.21 wt.%), Na_2O (0.07–1.13 wt.%, av. 0.60 wt.%), K_2O (0.05–0.35 wt.%, av 0.19 wt.%), CaO (0.07–0.10 wt.%, av. 0.41 wt.%), and Al_2O_3 (0–1.22 wt.%, av. 0.28 wt.%) and high contents of SiO_2 (87.47–93.35 wt.%, av. 90.86 wt.%) and H_2O (3.14–11.10 wt.%, av. 7.00 wt.%). The average Cs_2O contents in M1 are identical within uncertainties to the average Cs content obtained from the whole-rock data (~0.2 wt.%).

Type M2: Cs, Na, Al, K, and Ca-dominant zones occur in opal-A at stage V (Fig. 4). Quantitative EPMA spot analyses reveal vastly different elemental compositions in

This is the peer-reviewed, final accepted version for American Mineralogist, published by the Mineralogical Society of America.
The published version is subject to change. Cite as Authors (Year) Title. American Mineralogist, in press.
DOI: https://doi.org/10.2138/am-2022-8532. http://www.minsocam.org/

the different zones. The high Cs zone (av. 1.40 wt.% Cs_2O) can incorporate numerous Na_2O, K_2O, CaO, Al_2O_3, and H_2O, with average values of 1.93 wt.%, 1.28 wt.%, 0.65 wt.%, 5.32 wt.%, and 8.64 wt.%, respectively. Elemental compositions in the low Cs zone include averages of 90.11 wt.% SiO_2, 0.61 wt.% Na_2O, 0.30 wt.% K_2O, 0.23 wt.% CaO, 1.23 wt.% Al_2O_3, 6.62 wt.% H_2O, and 0.19 wt.% Cs. These elements' average contents in the low Cs zone in M2 correlate with that in M1 (Table A2).

Type M3 contains quartz cemented by amorphous opal with low Cs contents (Fig. 5). The lowest contents of Cs_2O (below EPMA detection limits), Na_2O (0.16 wt.%), K_2O (0.09 wt.%), CaO (0.04 wt.%), Al_2O_3 (0.55 wt.%), and H_2O (0.80 wt.%) were present in this type.

Based on the elemental compositions, we will call low Cs-bearing ore/geyserite (M1 in opal-CT and opal-A, and low Cs zone in M2 in opal-A), and high Cs-bearing ore/geyserite (high Cs zone in M2 in opal-A).

4.4 Nanoscale petrographic results using TEM

Sample DGJ-10A (Type M2) with high Cs contents (up to 2.89 wt.%) and low Cs contents (average 0.20 wt.%) (Table A2) was used to conduct TEM. EDS analysis demonstrated significant variations in Cs contents as a function of the mineral host (Fig. A3a, c). The area with low Cs contents is amorphous and disorganized (Fig. A3a, b). The well-defined lattice fringes evidenced the microcrystalline nature of particles with high Cs content, representing an interplanar spacing of 0.2 nm–0.25 nm

This is the peer-reviewed, final accepted version for American Mineralogist, published by the Mineralogical Society of America.
The published version is subject to change. Cite as Authors (Year) Title. American Mineralogist, in press.
DOI: https://doi.org/10.2138/am-2022-8532. http://www.minsocam.org/

(Fig. A3c–f).

5. Discussion

Macroscopically, most studies have reported enrichment of the amorphous silica opal-A in Cs, which might be explained by how Cs substitutes −OH based on whole-rock data because opal-A contains high H_2O contents (the correlation between Cs and H_2O is 0.75 in previous studies) (Fig. A4, Table A4) (Zheng et al., 1995; Zhao et al., 2006a, b, 2008, 2010; Luo et al., 2012; Zhou et al., 2013). The most striking observation from our measurements is that significant Cs content variation is extremely sensitive to the cation contents. The Cs shows a weak correlation with Na_2O, Al_2O_3, K_2O, SiO_2, and CaO in low Cs-ore, and an excellent occurs in the high Cs-bearing ore (Fig. 6a–e). However, this study did not obtain a good correlation between Cs and H_2O (Fig. 6f). The second observation of 2.89 wt.% Cs_2O is extensively higher than that of reported values of 1.55 wt.% (Zheng et al., 1995) and ~9000 ppm in this study based on whole-rock data (Table A1). Our results indicate that preliminary observations of mineral composition variations and the texture of Cs ore in the microstructure limit the interpretation based on whole-rock data. Therefore, our approach first explores the processes controlling the heterogeneous Cs distribution and enrichment from different ore-forming processes (migration–precipitation–enrichment–dissolution).

This is the peer-reviewed, final accepted version for American Mineralogist, published by the Mineralogical Society of America.
The published version is subject to change. Cite as Authors (Year) Title. American Mineralogist, in press.
DOI: https://doi.org/10.2138/am-2022-8532. http://www.minsocam.org/

5.1 The Cs migration from deep to shallow and ore precipitation mechanisms from geothermal fluids

Modern geothermal fluid mineralization is ongoing, and the geochemical characteristics of Cs-mineralizing fluids at stage V are summarized as follows: pH ~8.5 (Fig. A5a), temperature 85 °C (Fig. A5b), and NaCl–H_2O systems (Zhao et al., 2008). The mineralization temperature is 40 °C for stage III (Zhao et al., 2008). The excellent correlation between Cs and Cl in geothermal fluids (Zhao et al., 2006b; Wang et al., 2019) implies that both elements migrate together as CsCl.

The formation of amorphous silica and illite from geothermal fluids under typical Cs-mineralizing conditions was modeled using the PHREEQC thermodynamic parameters and the llnl.dat (Parkhurst and Appelo, 2013). Figure 7 shows the mineral saturation index at different pH and temperatures in the studies by Yan et al. (2019) and Zhao et al. (2007), who studied the elemental compositions of geothermal fluids in detail (Table A5). Amorphous silica precipitates at pH 6–9 and low temperatures <100 °C (Guidry and Chafetz, 2002). Based on computed saturation indexes (SI), the SI of amorphous silica is lower than 0 (SI < 0, no precipitation) because the solution is undersaturated (~100 ppm). However, large-scale amorphous silica formation is observed in the field, most likely caused by (1) the formation of ice (Channing and Butler, 2007) due to low temperatures (~−10°C) and high altitude (~5000 m) of the study area, and (2) the oversaturated Si concentrations in Li et al. (2006) of 100–600 ppm at 45 °C–84 °C causing silica acid to precipitate. A crucial clay mineral, illite,

This is the peer-reviewed, final accepted version for American Mineralogist, published by the Mineralogical Society of America.
The published version is subject to change. Cite as Authors (Year) Title. American Mineralogist, in press.
DOI: https://doi.org/10.2138/am-2022-8532. http://www.minsocam.org/

the secondary Al-bearing phase, is precipitated from the geothermal fluids under SI > 0. The most suitable physical parameters for illite precipitation are at pH ~7 and > 50 °C (Fig. 7, Table A5). The model results reproduce the field observation that illite coexisting with opal is common in geothermal systems (Boudreau, 1990; Smith et al., 2017). Amorphous silica formation is less sensitive to temperature and pH than illite, and simple cooling is more efficient for amorphous silica precipitation than illite. Furthermore, illite and opal layers indicate the physical conditions of geothermal fluid changes.

Additionally, Boudreau (1990) established a diagenesis model for clay preservation opal or devoid of dissolvable opal. This model considers conserving the dissolvable solid at a steady state with constant porosity and is simulated by applying the following equation.

$$F_b - \frac{F_m b(\infty)}{\rho_{m_{clay}}\left(1-\frac{b(\infty)}{\rho_{b_{opal}}}\right)} - \gamma\varphi D_s\left[\frac{k_s b(\infty)}{Ds\rho_{b_{opal}}}\right]^{\frac{1}{2}}(C_s - C_w) = 0 \text{ (Eq. 1)}$$

$$F_{er} = \frac{F_m\rho_{b_{opal}}}{\rho_{m_{clay}}} + [(\frac{F_m\rho_{b_{opal}}}{\rho_{m_{clay}}})^2 + (\gamma\varphi)^2 k_s D_s(C_s - C_w)]^{1/2}, \text{ (Eq. 2)}$$

where C_{sil} (mM) is the dissolved silica, b_{opal} is the solid opal (g cm^{-3} of total solids), and m_{clay} is an inert phase (g cm^{-3} of total solids). φ is the porosity, D_s is the tortuosity-corrected diffusion coefficient for dissolved silica (cm^2 y^{-1}), k_s is the rate constant for opal dissolution (y^{-1}), and C_s is the saturation concentration of dissolved silica. γ is the constant for unit conversion (0.0961 g $mmol^{-1}$), and $\rho_{b_{opal}}$ and $\rho_{m_{clay}}$ is the intrinsic density of opal and inert material clay (g cm^{-3}). F_b, F_m, and F_{er} are the

This is the peer-reviewed, final accepted version for American Mineralogist, published by the Mineralogical Society of America.
The published version is subject to change. Cite as Authors (Year) Title. American Mineralogist, in press.
DOI: https://doi.org/10.2138/am-2022-8532. http://www.minsocam.org/

input fluxes of opal, clay, and input rain, respectively, for which all incoming opal would dissolve and still succeed in saturating the porewater for a given set of parameter values. Table 2 lists the parameter values applied to the model. Geothermal fluids at approximately 80 °C have ~100 ppm (1.67 mmol/L) SiO_2 (Wang et al., 2015). Hence, C_s and C_w are 4.83 mmol/L and 1.67 mmol/L, respectively. The model indicates that opal dissolution is less noticeable as F_m increases (Fig. 7b); therefore, the clay mineral prevents amorphous silica dissolution.

5.2 The Cs-enrichment processes

5.2.1 Enrichment processes in low Cs-bearing ores

Silica sinters formed in modern geothermal systems under specific physical and chemical conditions primarily comprise amorphous silica opal-A (see the discussion in Section 5.1). The higher alkali and/or alkaline earth metal contents neutralize the negatively charged metastable SiO_2 particles and promote the coagulation of $SiO_2 \cdot H_2O$ gel (Visser, 2018). Therefore, the silica gel can coprecipitate with these elements (Cs in this study) in a disordered structure (Fig. A3b).

Amorphous silica is made up of the silanol group (Si–OH) and H_2O, including Si–OH$\cdots n H_2O$ (H_2O_{SiOH}, Type A molecular water), individual water molecules (H_2O_{mol}, Type B molecular water), −OH$\cdots n H_2O$ (Type A silanol group), and −OH (Type B silanol group) (Fig. A6a). Fourier transform infrared spectroscopy indicates the presence of water (Fig. A7), and Type A molecular water is much less mobile than

355 Type B (Zhuravlev, 2000). Essential property changes in opal-A and opal-CT are the
356 contents of H_2O and silicic bonds (siloxane bond, Si–OH and silanol bond, and Si–O–
357 Si). The total water content (Type A + Type B water) and Type B water content vary
358 significantly in opal-A and opal-CT, whereas opal-A contains a higher content of Type
359 A water than opal-CT (Table A5) (Day and Jones, 2008). Hence, the no correlation
360 between Cs and H_2O observed in this study indicates that there are no or only minor
361 differences in total water content in opal-A (av. 7.45 wt.%) and opal-CT (av. 7.00
362 wt.%) (Table A6).

363 The H_2O/Cs ratio decreases with increasing Cs content (Fig. A8a), reflecting a
364 condition with different water coordination numbers (CN) to cations. The negligible
365 contents of trivalent cations, such as Al, in low Cs-bearing ore and no apparent
366 relationship between positive and negative charges preclude Cs from being a charge-
367 balancing cation (Fig. A8c–e). The only explanation is that Cs forms a mobile outer-
368 sphere surface complex at the silica–water surface (Zhou et al., 2013). Deprotonation
369 of Si–OH (Types A and B silanol groups, Reactions 1 and 2) induces broken
370 crystallite edges with a negative charge, and the uptake of alkali ion Cs compensates
371 for the negative charge at the silica–water surface to yield a neutral suspension
372 (Reactions 3 and 4) (H site in Fig. A6a). The O atoms of the Si (Cs substitution −OH)
373 bind and coordinate the Cs. This mechanism was recognized in previous studies and
374 has been evidenced using ^{133}Cs NMR spectra of samples from the Targejia Cs-bearing
375 deposit (Zhou et al., 2013) and of Cs absorbed into silica gel (Kim et al., 1996 a, b).

This is the peer-reviewed, final accepted version for American Mineralogist, published by the Mineralogical Society of America.
The published version is subject to change. Cite as Authors (Year) Title. American Mineralogist, in press.
DOI: https://doi.org/10.2138/am-2022-8532. http://www.minsocam.org/

The low contents of Cs surrounded by a high-water CN with stronger hydrogen-bonded hydroxyls (Reaction 4) have been verified using ^{1}H NMR spectra by Zhou et al. (2013). Because surface deprotonation induces the charge and no permanent charge exists on the surface, the ability of Cs motion is closely related to the mobility of surface water (Kim et al., 1996a, b). Consequently, the Cs reactivity in an amorphous phase is because of a lower degree of ordering (Fig. A3b) and high-water CN (Fig. A8a). It is reasonable to infer that a poor Cs-bearing ore with high Cs motion moves easier at different mineralization stages (I–V) over time.

$$Si–OH \leftrightarrow Si\text{-}O^{-} + H^{+} \text{ (Reaction 1)}$$

$$Si–OH\cdots nH_2O \leftrightarrow Si–O^{-}\cdots nH_2O + H^{+} \text{ (Reaction 2).}$$

$$Si–O^{-} + Cs^{+} \leftrightarrow Si–OCs \text{ (Reaction 3)}$$

$$Si\text{-}O^{-}\cdots nH_2O + Cs^{+} \leftrightarrow Si–OCs\cdots nH_2O \text{ (Reaction 4)}$$

Why was high Cs content of whole-rock opal-A observed in past studies? Two reasons are plausible: (1) opal-A includes high H_2O content in previous studies, and (2) the high Cs-bearing ore coexists with opal-A (Type M2) in this study (see the discussion in Section 5.2.2).

5.2.2 Enrichment processes in high Cs-bearing ores

The Cs cation exchange capacity (CEC) for various minerals reported in the literature ranges from 0.5 wt.% to 8.0 wt.%. Montmorillonite reaches a maximum CEC, followed by illite, vermiculite, kaolinite, silica gel, boehmite, corundum, and

397 gibbsite (Table A7) (Kim et al., 1996a, b; Ejeckam and Sheeriff, 2005; Yuan et al.,
398 2020), the same as in this study. The good correlations between Cs and other
399 elements, especially Al (Fig. 6b–e), indicate that Cs enrichment is related to these
400 elements.

401 Three parameters affect the CEC. (1) the layer charge caused by substituting
402 lower charged cations (Al^{3+}, Mg^{2+}) for Si^{4+} in the tetrahedral or octahedral sheets
403 creates a negative charge to absorb Cs (Kim et al., 1996a, b). In the high Cs-bearing
404 ore, CEC increases from 0.42 wt.% to 2.89 wt.% as Al_2O_3 increases from 1.37 wt.%
405 to 10.33 wt.%. The analysis using the charge balance method rules out Ca^{2+}
406 substitution for Si^{4+} because the positive and negative charges are unbalanced (Fig.
407 A8b–d). Cations were adsorbed preferentially close to the tetrahedral sites, where
408 $[AlO_4]^{5-}$ tetrahedra produce a local charge imbalance, and Cs in such environments is
409 tightly bound to and coordinated by O atoms of the $[AlO_4]^{5-}$ tetrahedra (such as the K
410 site in Fig. A6b). Additional sources of surface charge attract Cs more effectively
411 (Guven, 1988). (2) The layer charge from mineral constructs, such as 1:1 vs. 2:1 layer
412 structures and the dioctahedral vs. trioctahedral. 1:1 layer structure, has a low CEC
413 due to the lack of exchangeable interlayer cations compared to the 2:1 layer structure
414 (Ejeckam and Sheeriff, 2005). The significant structural differences (high-degree
415 disorder vs. high-degree order, Fig. A3) between Cs-bearing ore and barren ores
416 significantly affect the CEC. (3) The absorption site is tightly bound to the basal
417 oxygen atoms (C1 site) and loosely bonded to H_2O molecules (C2 site), and the CEC

This is the peer-reviewed, final accepted version for American Mineralogist, published by the Mineralogical Society of America.
The published version is subject to change. Cite as Authors (Year) Title. American Mineralogist, in press.
DOI: https://doi.org/10.2138/am-2022-8532. http://www.minsocam.org/

418 is higher for C1 than C2 (Kim et al., 1996a, b; Ejeckam and Sheeriff, 2005). Edge
419 sites and basal crystallite surfaces (or planar and surface sites) are essential adsorption
420 sites for Cs in illite, as evidenced using ^{133}Cs NMR spectra (Kim et al., 1996b). The
421 Cs motion ability in the high Cs-bearing ore should be lower than in the low Cs-
422 bearing ore and is attributable to a low water CN (Fig. A8a), permanent charge caused
423 by Al (Fig. A8c), and high-degree order (Fig. A3d–f). In short, elemental
424 compositions and mineral constructs influence the enrichment mechanism and degree
425 of Cs in low and high Cs ores.
426
427 **5.2.3 The behavior of other trace elements in Cs-bearing ores**
428 The contents of Cs (up to ~5 ppm), Li (~5 ppm), and HBO_4 (~100 ppm) in
429 geothermal or ore-forming fluids of the Tibetan geothermal area are several to dozens
430 of times the average abundance of the Earth's crust (Wang et al., 2019). Note the high
431 Li and B contents in geothermal fluids compared to Cs (Wang et al., 2019), but Li and
432 B are not in geyserite (Li, 0–44 ppm; B, 0–400 ppm, and Cs, Table A3). The
433 enrichment factor of Li and B is several times higher than that of fluids (Li up to nine
434 times; B up to four times). The contents of Be (~0.1 ppm), Ga (~0.1 ppm), Rb (~0.6
435 ppm), and Sr (~0.2 ppm) (Wang et al., 2019) in geothermal fluids are negligible, but
436 they can be enriched hundreds to thousands of times in ore (Be, 0.6–600 ppm, up to
437 6000 times; Ga, 0–585 ppm, up to 5850 times; Rb, 20–300 ppm, 33–500 times; Sr, 0–
438 625 ppm, up to 3000 times). The results imply the property of adsorption selectivity

This is the peer-reviewed, final accepted version for American Mineralogist, published by the Mineralogical Society of America.
The published version is subject to change. Cite as Authors (Year) Title. American Mineralogist, in press.
DOI: https://doi.org/10.2138/am-2022-8532. http://www.minsocam.org/

439 of the ore, indicating the adsorption capacity of Be^{2+}, Ga^{3+}, Rb^{+}, Sr^{2+}, and Cs^{+} and no
440 adsorption capacity of Li^{+} and B^{3+}. A poor correlation between Li, Be, B, Ga, and Cs
441 (Fig. A9a, b, c, d) and close relationships between Rb, Sr, and Cs (Fig. A9e, f) were
442 identified. Rb, Sr, and Cs are the most common elements. They show suitable
443 corresponding concentrations in the LCT-family pegmatites (Černý, 1978), attributing
444 to similar geochemical properties among these elements, such as their similar atomic
445 radii of Rb^{+} (1.52 Å), Sr^{2+} (1.18 Å), and Cs^{+}, (1.67 Å), but inconsistent values of Be^{2+}
446 (0.16 Å) and Ga^{3+} (0.47 Å) (Shannon, 1976).
447

448 ## 5.3 The dissolution and reprecipitation of Cs ores

449 Clay minerals (illite) disappeared accompanied by Cs content reduction from
450 stage V to stage IV (0–4 ka to 4–17 ka) in this study. In stages I and II (>99 ka), even
451 though clays (kaolinite) reformed under weathering, there was no reenrichment of Cs
452 in clay minerals. Therefore, the ores formed in the early stages were isolated from the
453 Cs aqueous surroundings and could be affected by the uplifted Tibet. Tectonic and
454 deep magmatic activities control the hot-spring Cs deposit formation, corresponding
455 to the plateau's uplift (Tong et al., 1981). Therefore, extreme Cs enrichment only
456 happened in the latest stage (< 17 ka), especially in Meghalayan (< 4ka). A common
457 mechanism for phase transformation from amorphous silica to crystalline quartz is
458 dissolution–reprecipitation (Lynne et al., 2007; Day and Jones, 2008). The mineral
459 dissolution–reprecipitation process produces a high-degree order in amorphous silica

This is the peer-reviewed, final accepted version for American Mineralogist, published by the Mineralogical Society of America.
The published version is subject to change. Cite as Authors (Year) Title. American Mineralogist, in press.
DOI: https://doi.org/10.2138/am-2022-8532. http://www.minsocam.org/

460 (Langer and Flörke, 1974). The disappearance of illite because of dissolution induces
461 Cs to be excluded from the ore, and this point is evidenced below.

462 Geothermal fluids loaded the source of the massive metallogenic mass. What
463 types of fluids cause mineral dissolution in early mineralization? There are no active
464 geothermal fluids in the early stages, so the only fluid is meteoric water. The
465 reconstructed Holocene climate development of Nam Co, central Tibet, shows (1)
466 high rainfall and meltwater input at 7.2–5.4 ka, (2) drier climate with less monsoonal
467 precipitation, higher evaporation rates at 5.4–4.0 ka, (3) the driest periods were
468 recorded at 4.0–1.4 ka, (4) increased precipitation and runoff at 1.4–0.8 ka, and (5)
469 intense evaporation at 0.8 ka to present (Mügler et al., 2010). In the following section,
470 one chemical system, meteoric water, was modeled to examine how temperature and
471 pH affect mineral dissolution and reprecipitation under the following conditions:
472 temperature of 0 °C–85 °C and pH of 5–9.

473 A dynamic balance between supply, transport processes (e.g., burial), and
474 dissolution determines the magnitude of mineral accumulation.

475 (1) Dissolution process

476 The Dissolution rates of natural illite (r_{illite}) and amorphous silica (r_{am}) were
477 calculated using empirical Eq. 1 (Köhler et al., 2003) and Eq. 2 (Rimstidt et al., 2016)
478 and were impacted by pH, temperature, and ion activity.

479 $$r_{illite} = A_H \exp\left(\frac{-E_{AH^+}}{RT}\right) a_{H^+}^{0.6} + A_{H_2O} \exp\left(\frac{-E_{AH_2O}}{RT}\right) + A_{OH} \exp\left(\frac{-E_{AOH^-}}{RT}\right) a_{OH^-}^{0.6}, \quad \text{(Eq. 3)}$$

480 where A_H, A_{H2O}, and A_{OH} are pre-exponential factors of 2.2×10^{-4}, 2.5×10^{-13},

This is the peer-reviewed, final accepted version for American Mineralogist, published by the Mineralogical Society of America.
The published version is subject to change. Cite as Authors (Year) Title. American Mineralogist, in press.
DOI: https://doi.org/10.2138/am-2022-8532. http://www.minsocam.org/

and 0.27 mol m^{-2} s^{-1}, respectively. E_{AH+}, E_{AH2O}, and $E_{A,\ OH-}$ designate the apparent activation energies of 46, 14, and 67 kJ mol^{-1}, respectively.

$$r_{Am} = 14.62(10^{-(\frac{77400}{2.303R})(\frac{1}{T})}) + 8.95(10^{-(\frac{77700}{2.303R})(\frac{1}{T})})(\frac{m_{Na^+}^{0.490}}{m_{H^+}^{0.377}}) \quad \text{(Eq. 4)}$$

where m_{Na+} (mol $kg^{-}1$) is the sodium (Na) concentration and m_{H+} is the hydrogen ion activity (a_{H+}).

Amorphous silica is more soluble than illite under the investigated conditions (Fig. 8a) because it has a higher dissolution rate than illite, and the lowest illite dissolution rate was observed at pH 6–9.

(2) Reprecipitation process

Meteoric water–rock interaction modeling involving conventional reaction path simulations where water of meteoric origin was allowed to react with rock in steps is described in detail by Kleine et al. (2018). Water was specified as an initial condition to simulate the infiltration of meteoric water into the rock (Table 2). The solid part of the model domain is obtained from the rock compositions of amorphous silica opal-A + clay (Table 2). As both parameters at the early mineralization stage are unknown, simulations were run for pH 5 (average pH of meteoric water) to 9 (average pH of geothermal fluids) and 40 °C (mineralization temperature of stage III) to 85 °C (mineralization temperature of stage V) (Table 2, Fig. 8b). Amorphous silica was allowed to precipitate under specific conditions, consistent with findings that amorphous silica formation can occur over several temperatures and pH values (see the discussion in Section 5.1). However, illite could precipitate when the water–rock

interaction reaches a specific degree (at least 10^{-4} mol rock per kg solution), implying that illite re-forms only if a specific amount of rock dissolution supplies enough elements. At low temperatures (<100 °C), an increase in temperature has no or negligible effect on the mineralization process. However, a pH shift to an alkaline level can promote amorphous silica accumulation precipitation. Furthermore, illite formation is challenging because of the necessary element supply for high water–rock interaction at alkaline pH (Fig. 8b). Compared to geothermal fluids containing high contents of Na and K (enough supply), the dissolution replenishment elemental contents are insufficient for illite re-formation in the early stage.

The meteoric water–rock interaction modeling indicates that clay formed at a late stage and redissolved in meteoric water. Amorphous silica can re-form owing to its chemical properties, and clay might impede dissolution.

6. Implications for Geothermal Fluid Mineralization and Elemental Extraction and Use

Geothermal fluid mineralization is vital for alkaline elements, such as Li (Benson et al., 2017; Guo et al., 2019) and Cs (Zheng et al., 1995). Hydrothermal fluids leach alkaline elements from host rocks and are structurally bound in clay and amorphous silica. These deposits have gained attention due to the high-speed mineralization compared to pegmatite-type rare metal deposits (Guo et al., 2019). This study presents an excellent example of a modern ore-forming process in the

Targejia area to study the alkaline elemental migration–precipitation–enrichment–preservation mechanisms. Detailed petrographic and geochemical studies revealed two primary ore growth minerals (amorphous silica and clay). The average Cs content in amorphous silica for low Cs-bearing ore, including Type M1 in opal-A and opal-CT, and low Cs zone in Type M2 in opal-A, is approximately 0.2 wt.%. The highest enrichment degree of Cs in clay is up to 2.89 wt.%. Two enrichment mechanisms cause the different enrichment degrees of different minerals. One is that Cs substitutes −OH of amorphous silica, and the other is that Cs is absorbed by a negative charge created by $A1^{3+}$ substituting more highly charged cations (Si^{4+}). The mineral saturation index model and meteoric water–rock interaction model indicate that mineral formation and disappearance reflect a dynamic physical–chemical condition in the fluid system. Such a process might have occurred in many geothermal deposits worldwide. Our observations provide new insights into elemental extraction and use under geothermal conditions.

CRediT authorship contribution statement

WW: Methodology, Formal analysis, Investigation, Writing - Original Draft; SYJ: Conceptualization, Resources, Supervision, Funding acquisition, Writing - Review & Editing; HZW: Methodology, Resources, Writing - Review & Editing.

Declaration of competing interest

The authors declare that they have no known competing financial interests or personal relationships that could have appeared to influence the work reported in this

paper.

Data and materials availability

All the data used in this paper are either listed as Table 1 and 2 in the main text or as an Appendix Supplementary Figures and Tables attached to this paper, and are also available from the corresponding author upon request.

Acknowledgments

This study was financially supported by the National Natural Science Foundation of China (nos. 42103063 and 92162323), the State Key Laboratory of Geological Processes and Mineral Resources, China University of Geosciences (No. MSFGPMR03-2), and Key Laboratory of Mineralogy and Metallogeny, Guangzhou Institute of Geochemistry, Chinese Academy of Sciences (No. KLMM20200203). We thank Yao Zhao and Yibo Lin for helping with sample collection. We also thank Barbara Kleine for help in geochemical modeling.

References

Benson T.R., Coble M.A., Rytuba J.J., Mahood G.A. 2017. Lithium enrichment in intracontinental rhyolite magmas leads to Li deposits in caldera basins. Nat. Commun. 8. 270.

Boudreau B.P., 1990. Modelling early diagenesis of silica in non-mixed sediments.

Deep-sea Res. 37, 1543-1567.

Černý P., 1978. The tanco pegmatite at Bernic Lake, Maintiva X. Pollucite: present status of theanalcime-pollucite series. Can. Mineral. 16, 325-333.

Channing A. and Butler I.B., 2007. Cryogenic opal-A deposition from Yellowstone hot springs. Earth Planet. Sci. Lett. 257, 121-131.

Day R. and Jones B., 2008. Variations in water content in opal-A and opal-CT from geyser discharge aprons. J. Sediment. Res. 78, 301-315.

Ejeckam R.B. and Sherriff B.L., 2005. A ^{133}Cs, ^{29}Si and ^{27}Al MAS NMR spectroscopic study of Cs absorption by clay minerals: implications for the disposal of nuclear waste. Can. Mineral. 43, 1131-1140.

Guo X.H., Zheng M.P., Liu X.F., Ye Z. and Pu L.Z., 2008. Saline cesium resource and prospect of its exploitation and utilization in Tibet. Salt & Chem. Industry 37, 8-12.

Guo W.M., Ma S.C., Sun Y., Zhao Z., Zhong H.R., Yao L.S. 2019. Characteristics and significance of rare metal mineralization in hot-springs of Thengchong area, Yunnan, Acta Geol. Sin., 93, 1321-1330.

Guidry S. A. and Chafetz H. S., 2002. Factors governing subaqueous siliceous sinter precipitation in hot springs: examples from Yellowstone National Park, USA. Sediment. 49, 1253-1267.

Han Y.X., Fang X.M., Zhao T.L., Bai H.Z., Kang S.C. and Song L.C., 2009. Suppression of precipitation by dust particles originated in the Tibetan Plateau.

588 Atmo. Environ., 43, 568-574.

589 Hou Z.Q., Li Z.Q., Qu X.M., Gao Y.F., Hua L.C., Zheng M.P., Li S.R. and Yuan
590 W.M., 2001. The uplifting processes of the Tibetan Plateau since 0.5 Ma B. P.-
591 evidence from hydrothermal activity in the Gangdise belt. Sci. China Ser. D 44,
592 35-44.

593 Kastner M., Keene J.B. and Gieskes J.M., 1977. Diagenesis of siliceous oozes-1:
594 chemical controls on the rate of opal-A to opal-CT transformation- an
595 experimental study. Geochim. Cosmochim. Ac. 41, 1041-1059.

596 Kim Y., Cygan R. and Kirkpatrick R.J., 1996a. ^{133}Cs NMR and XPS investigation of
597 cesium absorbed on the clay minerals and related phases. Geochim. Cosmochim.
598 Ac. 60, 1041-1052.

599 Kim Y., Kirkpatrick R.J. and Cygan R., 1996b. ^{133}Cs NMR study of cesium on the
600 surfaces of kaolinite and illite. Geochim. Cosmochim. Ac. 60, 4059-4074.

601 Kleine B.I., Stefánsson A., Halldórsson S.A., Whitehouse M.J., Jónasson K., 2018.
602 Silicon and oxygen isotopes unravel quartz formation processes in the Icelandic
603 crust. Geochem. Persp. Let. 7, 5-11

604 Langer K., and Flörke O.W., 1974. Near infrared absorption spectra (4000-9000 cm)
605 of opals and the role of ‘‘water’’ in the $SiO_2 \cdot nH_2O$ minerals. Fortschritteder
606 Mineralogie, 52, 17-51.

607 Li Z.Q., 2002. Present Hydrothermal Activities during Collisional Orogenics of the
608 Tibetan Plateau. Beijing.

609 Li Z.Q., Hou Z.Q., Nie F.J. and Yang Z.S., 2006. Enrichment of Element Cesium
610 during Modern Geothermal Action in Tibet, China. Acta Geol. Sin. 80, 1457-
611 1464.
612 Li Z.Q., Hou Z.Q., Nie F.J. and Meng X.J., 2005. Characteristics and distribution of
613 the partial melting layers in the upper crust: evidence from active hydrothermal
614 fluid in the southern Tibet. Acta Geol. Sin. 79, 68-76.
615 Li Y.L., Wang C.S., Dai J.G., Xu G.Q., Hou Y.L. and Li X.H., 2015. Propagation of
616 the deformation and growth of the Tibet-Himalayan orogen: A review. Earth-Sci.
617 Rev. 143, 36-61.
618 Luo W., Zhao Y.Y., Ren Z.F. and Li Y.T., 2012. ^{1}H and ^{29}Si MAS NMR of the
619 geyserite in Tibetan Gulu area, China. J. Salt Lake Res. 20, 43-62.
620 Lynne B.Y., Campbell K.A., James B.J., Browne P.R.J. and Moore J., 2007. Tracking
621 crystallinity in siliceous hot-spring deposits. Am. J. Sci. 307, 612-641.
622 Lynne B.Y., 2015. Impact of three common post-depositional environmental settings
623 on siliceous sinter diagenesis: an eight-year experiment. J. Volcanol. Geotherm.
624 Res. 292, 84-101.
625 Mügler I., Gleixner G., Günther F., Maüsbacher R., Daut G., Schütt B., Berking J.,
626 Schwalb A., Schwark L., Xu B., Yao T., Zhu L., Yi C., 2010. A multi-proxy
627 approach to reconstruct hydrological changes and Holocene climate development
628 of Nam Co, Central Tibet. J. Paleolimnol. 43, 625-648.
629 Parkhurst D.L. and Appelo C.A.J., 2013. Description of input and examples for

630 PHREEQC version 3: a computer program for speciation, batch-reaction, one-
631 dimensional transport, and inverse geochemical calculations. U.S. Geological
632 Survey Water-Resources Investigations Report.
633 Rimstidt J.D., Zhang Y.L. and Zhu C., 2016. Rate equations for sodium catalyzed
634 amorphous silica dissolution. Geochim. Cosmochim. Ac. 195, 120-125.
635 Rui Z.Y. and Shen J.Z., 1992. Research progress of hot spring type ore deposits. Bull.
636 Miner. Petrol. Geochem. 3, 147-152.
637 Shannon R.D., 1976. Revised effective ionic radii and systematic studies of
638 interatomic distances in halides and chalcogenides. Acta. Crystallogr. A. 32, 751-
639 767.
640 Sherlock R.L. and Lehrman N.J., 1995. Occurrences of dendritic gold at the
641 McLaughlin mine hot-spring gold deposit. Miner. Deposita. 30, 323-327.
642 Sherlock R.L., 2005. The relationship between the McLaughlin gold-mercury deposit
643 and active hydrothermal systems in the Geysers-Clear Lake area, northern Coast
644 Ranges, California. Ore Geol. Rev. 26, 349-382.
645 Shi J., Jin, Z., Liu Q., Fan T. and Gao Z., 2021. Sunspot cycles recorded in Eocene
646 lacustrine fine-grained sedimentary rocks in the Bohai Bay Basin, eastern China,
647 Global Planet. Change, 103614.
648 Tan H.B., Zhang Y.F., Zhang W.J., Kong N., Zhang Q. and Huang J.Z., 2014.
649 Understanding the circulation of geothermal waters in the Tibetan Plateau using
650 oxygen and hydrogen stable isotopes. Appl. Geochem. 51, 23-32.

T'ung W. and Zhang J., 1981. Characteristics of geothermal activities in Xizang Plateau and their controlling influence on Plateau's tectonic model. In: Gordon, Breach, eds. Geological and Ecological studies of the Qinghai-Xizang Plateau. New York: Science Publishers Inc. 841-846.

Tong W., Zhang M.T., Zhang Z.F., Liao Z.J., You M.Z., Zhu M.X., Guo J.Y., and Liu S.B. 1981, Geotherm in Xizang, Beijing: Science press.

Van Cappellen P., Dixit S. and van Beusekom J., 2002. Biogenic silica dissolution in the oceans: reconciling experimental and field-based dissolution rates. Global Biogeochem. Cycles 16, 23-1-23-10.

Visser J.H.M., 2018. Fundamentals of alkali-silica gel formation and swelling: Condensation under influence of dissolved salts. Cement Concrete Res. 105, 18-30.

Wang W., Wei H.Z., Jiang S.Y., Tan H.B., Eastoe C.J., Williams-Jones A.E., Hohl S.V. and Wu H.P., 2019. The origin of rare alkali metals in geothermal fluids of southern Tibet, China: A silicon isotope perspective. Sci. Rep. 9, 7918.

Wang Z.B., Shen L.C., Liang Z.B., Jiang Z.L. and Liao Y., 2015. Characteristics of hydrochemical compositions and stable carbon isotope of natural water in the Daggyia geothermal field, Tibet, China. Carsologica Sin. 34, 201-208.

Yan K.T., Guo Q.H. and Liu M.L., 2019. Geochemical anomalies of arsenic and its speciation in Daggyai geothermal springs, Tibet. J. Jilin Univ. (Earth Sci. Ed.) 49, 548-558.

672 Yang, S.Y., Jiang, S.Y., Mao, Q., Chen, Z.Y., Rao, C., Li, X.L., Li, W.C., Yang, W.Q.,
673 He, P.L. and Li, X., 2022. Electron probe microanalysis in geosciences: Analytical
674 procedures and recent advances. Atomic Spectroscopy 43, 186-200.
675 Yuan T.Y., Chen Q.D. and Shen S.H., 2020. Adsorption of cesium using mesoporous
676 silica gel evenly doped by Prussian blue nanoparticles. Chinese Chem. Lett. 31,
677 2835-2838.
678 Zeeck L.R., Monecke T., Reynolds T.J., Tharalson E.R., Pfaff K., Kelly N.M. and
679 Hennigh Q.T., 2021. Textural characteristics of Barren and Mineralized colloform
680 quartz bands at the low-sulfidation epithermal deposits of the Omu Camp in
681 Hokkaido, Japan: implications for process resulting in Bonanza-Grade precious
682 metal enrichment. Econ. Geol. 116, 407-425.
683 Zhang, R.X. and Yang, S.Y., 2016. A mathematical model for determining carbon
684 coating thickness and its application in electron probe microanalysis. Microscopy
685 and Microanalysis 22, 1374-1380
686 Zhao Y.Y., Zhao X.T. and Ma Z.B., 2006a. Study on chronology for hot spring typed
687 Cs-deposite of Targjia, Tibet. Acta Petrol. Sin. 22, 717-724.
688 Zhao Y.Y., Nie F.J., Hou Z.Q., Li Z.Q., Zhao X.T. and Ma Z.B., 2006b. Isotope
689 characteristics and formation process of hot spring type cesium deposit in
690 Targejia, Tibet. Mineral Deposits 25, 614-619.
691 Zhao Y.Y., Han J.Y., Guo L.H., Qian Z.H., Zhou Y.Z., Nie F.J. and Li Z.Q., 2008.
692 Characteristics and geological significance of mineralogy and fabrics for the hot

693 spring cesium deposit occurring within the Targejia district, Tibet. Acta Petrol.
694 Sin. 24, 519-530.
695 Zhao Y.Y., Zhao X.T., Ma Z.B. and Deng J., 2010. Chronology of Gulu hot spring
696 cesium deposit in Nagqu, Tibet and it geological significance. Acta Geol. Sin. 84,
697 211-220.
698 Zhuo B., Ren E., Sherriff B.L. and Yao Y., 2013. Multinuclear NMR study of Cs-
699 bearing geyserites of the Targejia hot spring cesium deposit in Tibet. Am. Mineral.
700 98, 907-913.
701 Zheng M.P., Wang Q.X., Duo J., Liu J., Ping Cuo, W.J. and Zhang S.C., 1995. A New
702 Type of Hydrothermal Deposit- Cesium- Bearing Geyserite in Tibet. Geological
703 Publishing House, Beijing (in Chinese).
704 Zhong D.L, and Ding L., 1996. Uplifting process and mechanism of Qinghai-Xizang
705 (Tibetan) Plateau. Sci. China 26, 289-295 (in Chinese).
706 Zhuravlev L.T., 2000. The surface chemistry of amorphous silica. Zhuravlev model.
707 Colloids Surf. A 173, 1-38.
708
709

710 FIGURE AND TABLE CAPTIONS

711 **Figure 1.** (a) Hot-spring deposits distributed globally; (b) A geological map of Tibet;
712 (c) A geological map of the Targejia deposit (modified by Zheng et al., 1995); (d) A
713 simplified geological section shows the five mineralization stages in the Targejia

district (modified by Zhao et al., 2008); (f) A field photo of stage III to V for Targejia.

Figure 2. Photomicrographs of textures (a–d) and SEM images (e–h) of ore samples from Targejia. (a, e) Type M1 in colloid opal-CT and opal-A; (b, c, f, g) Type M2 of zones comprising alternating, irregular concentric bands or shells of color in opal-A; (d, h) Type M3 of quartz cemented by amorphous opal.

Figure 3. Electron probe microanalyzer (EPMA) mapping of Type M1 (from Fig 2a, e), with distribution maps of Si, Na, Al, K, Ca, and Cs.

Figure 4. Electron probe microanalyzer (EPMA) mapping of Type M2 (from Fig 2b, c, f, g), with distribution maps of Si, Na, Al, K, Ca, and Cs.

Figure 5. Electron probe microanalyzer (EPMA) mapping of Type M3 (from Fig. 2d, h), with distribution maps of Si, Na, Al, K, Ca, and Cs.

Figure 6. Correlation diagrams between Cs_2O and (a) SiO_2, (b) Na_2O, (c) K_2O, (d) Al_2O_3, (e) CaO, (f) H_2O. The blue line represents the correlation in low Cs-bearing ore. The red line represents the correlation in the high Cs zone in high Cs-bearing ore. The light green area denotes the area of low Cs-bearing ore.

Figure 7. (a) Mineral saturation indices (SI) with different pH values and temperatures; (b) The relationship between clay input (F_m) and the ratio of the rain and opal inputs (F_{er}/F_m).

Figure 8. (a) The dissolution rates of amorphous silica and illite at pH 1–14; (b) Minerals formed upon meteoric water–rock interaction.

735 **Table 1.** Parameter values applied in the diageneses model.

736 **Table 2.** Input values of meteoric water and rock for geochemical meteoric water–

737 rock modeling.

738

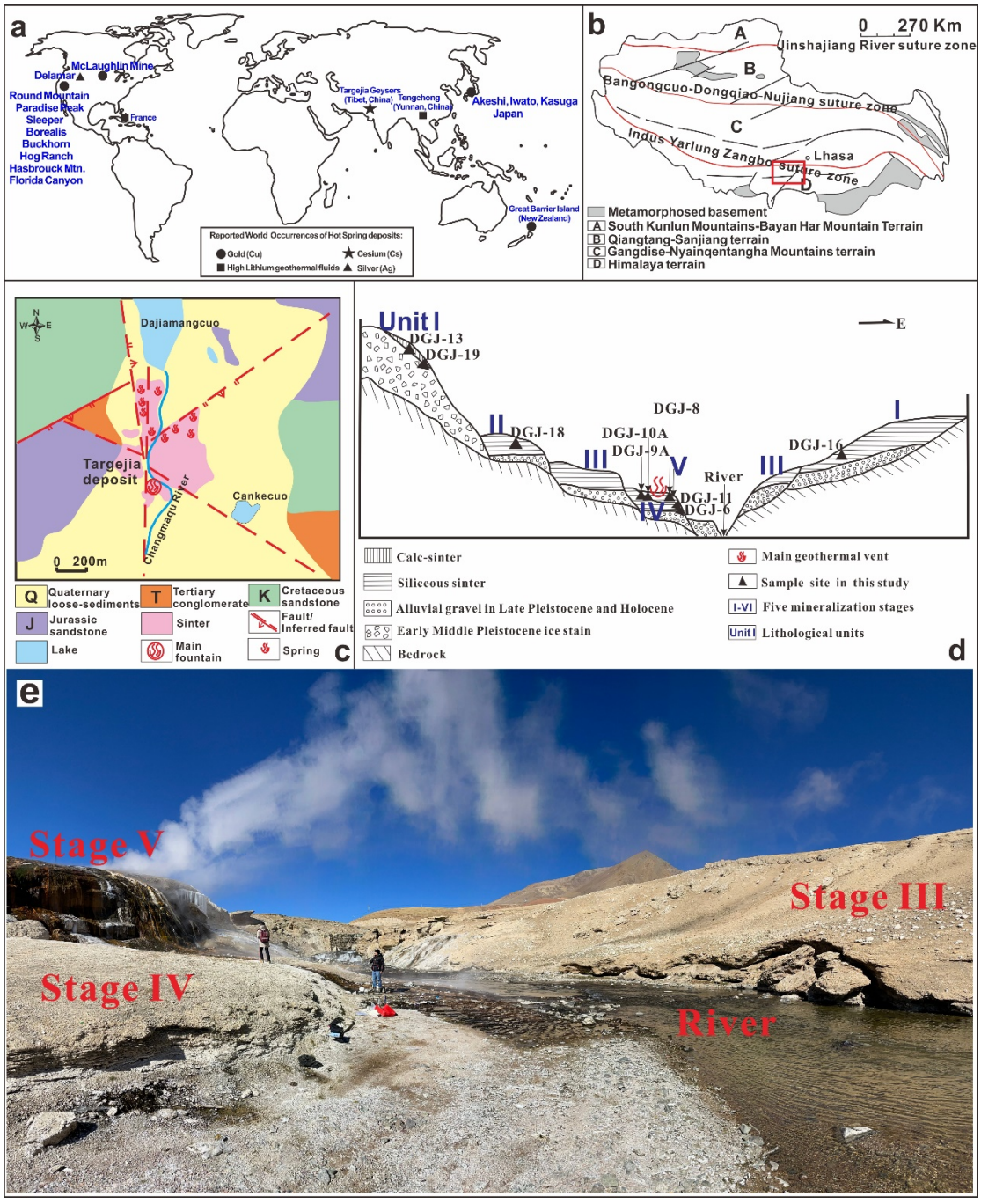

Figure 1. (a) Hot spring deposits distributed in the world; (b) The geological map of Tibet; (c) The geological map of Targejia deposit (modified by Zheng et al., 1995); (d) Simplified geological section shows the five mineralization stages in the Targejia district (modified by Zhao et al., 2008); (f) the field photo of stage III to V for Targejia.

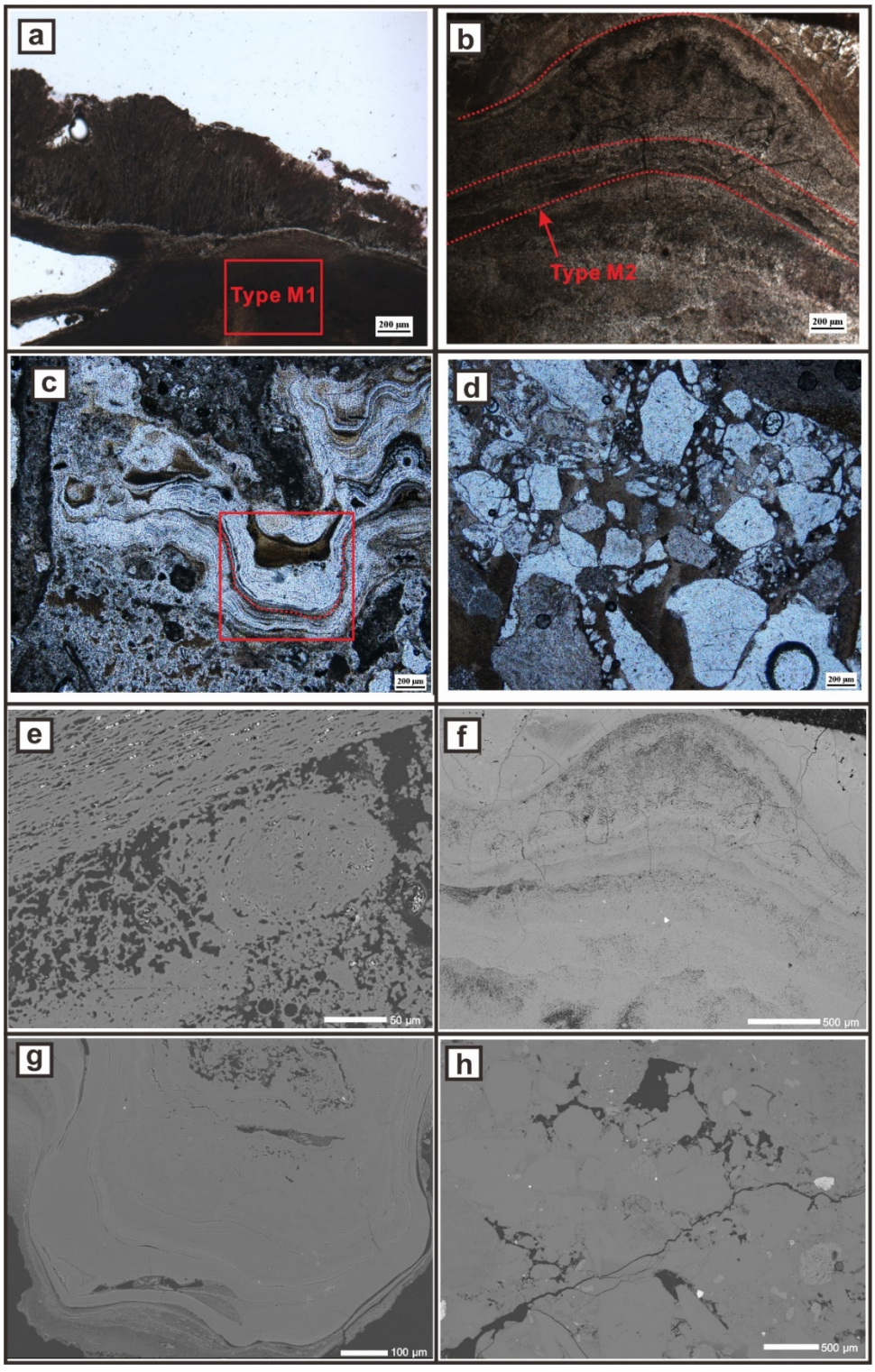

Figure 2. Photomicrographs of textures (a-d) and SEM characteristics (e-h) present in ore samples from the Targejia. (a, e) type M1 in colloid opal-CT and opal-A; (b, c, f, g) type M2 of zones consist of alternating, irregular concentric band or shells of color in opal-A; (d, h) type M3, quartz cemented by amorphous opal.

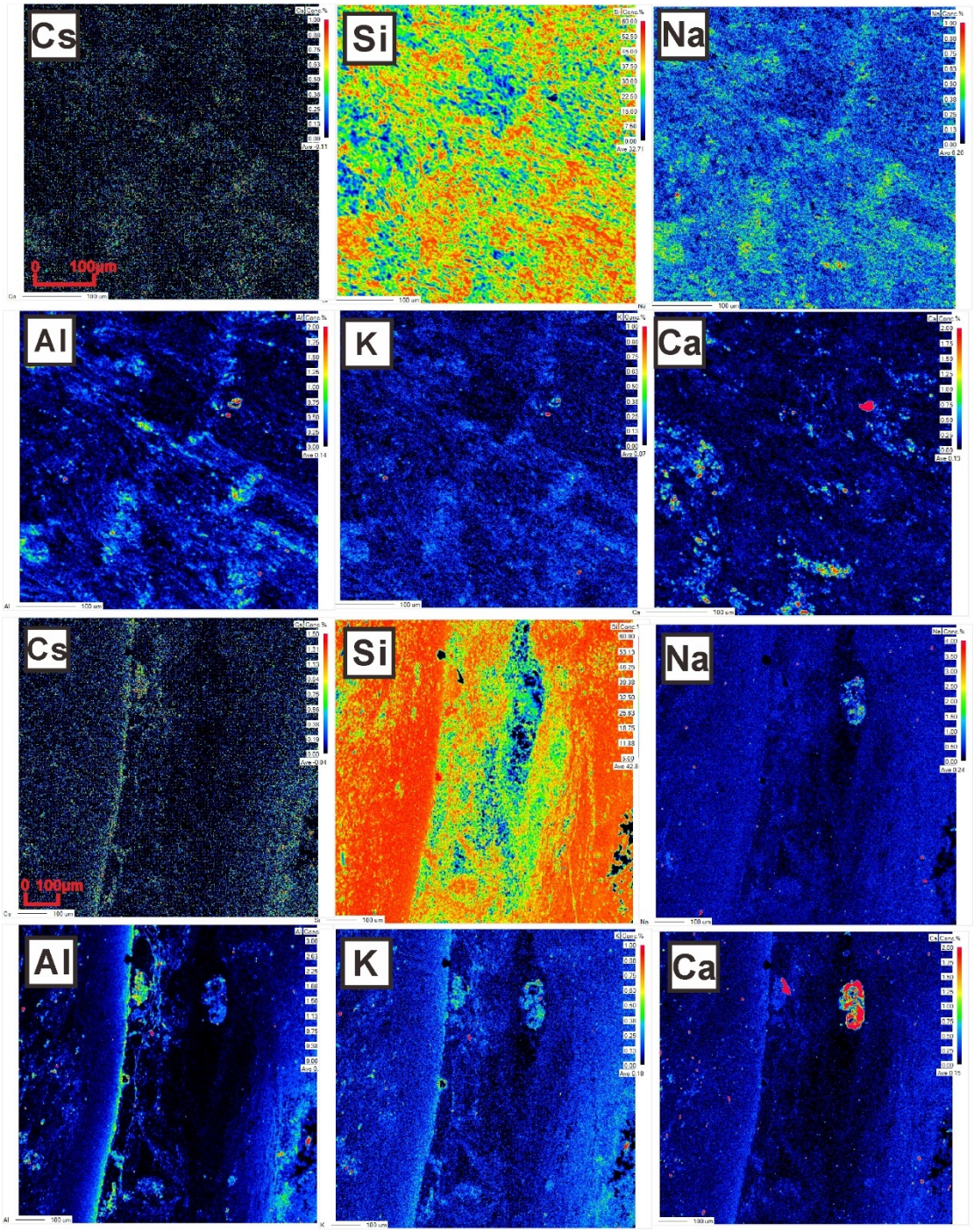

Figure 3. EPMA mapping of type M1 (from Fig 3a, e) with distribution map of Si, Na, Al, K, Ca and Cs, respectively.

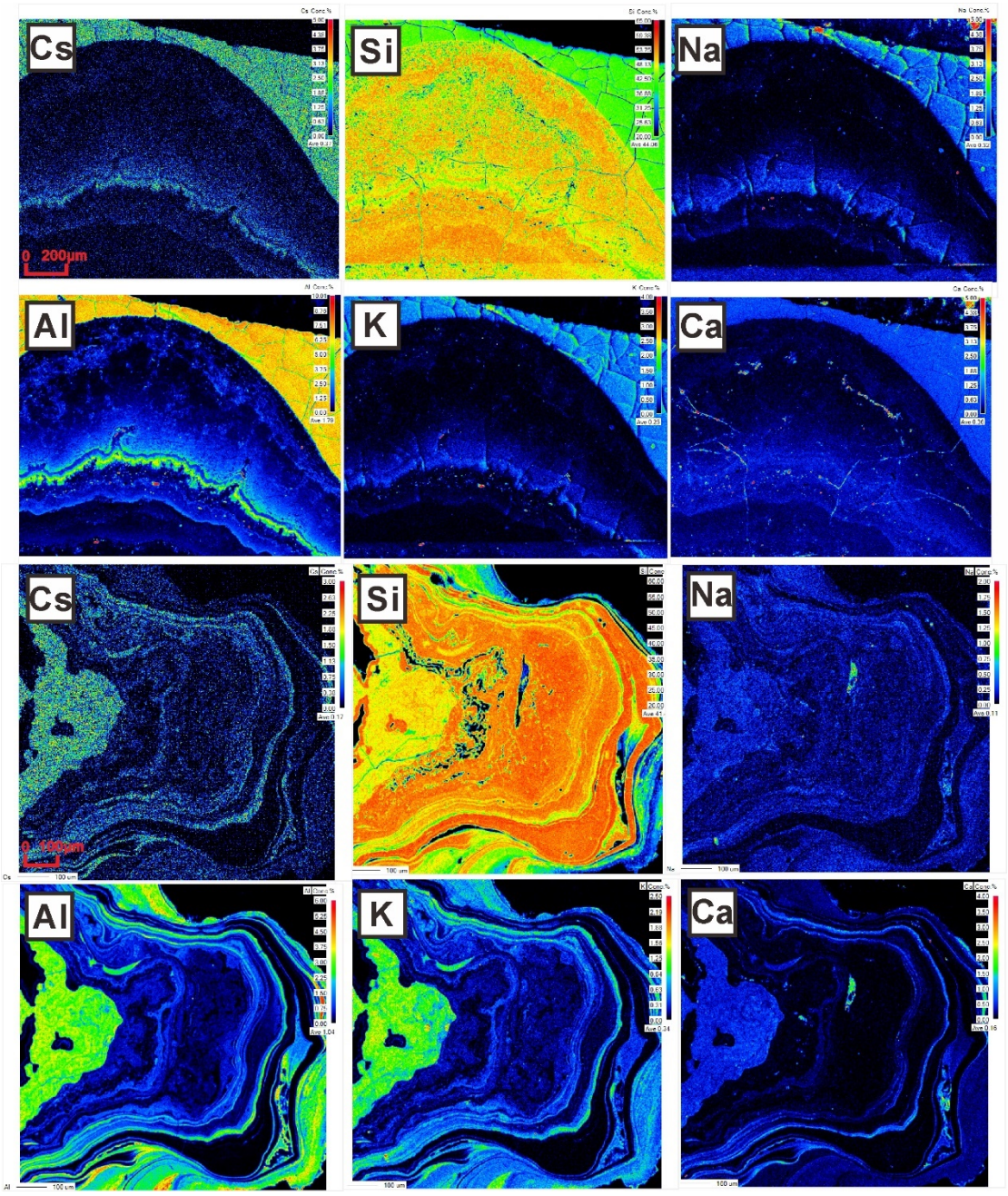

Figure 4. EPMA mapping of type M2 (from Fig 3b, c, f, g) with distribution map of Si, Na, Al, K, Ca and Cs, respectively.

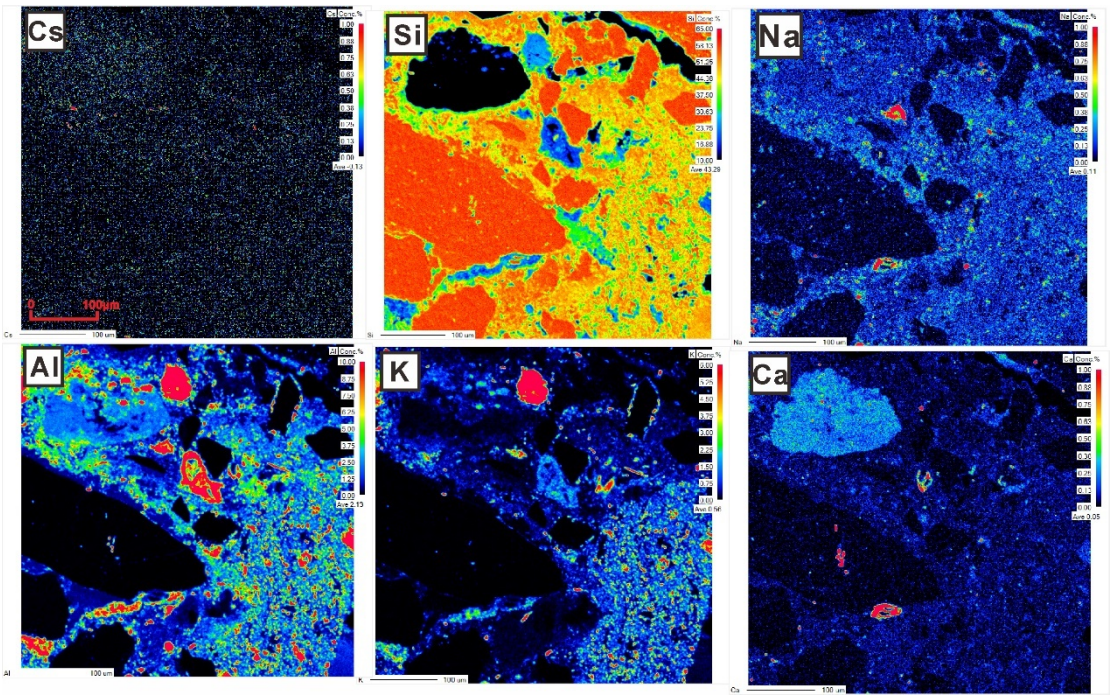

Figure 5. EPMA mapping of type M3 (from Fig. 3d, h) with distribution map of Si, Na, Al, K, Ca and Cs, respectively.

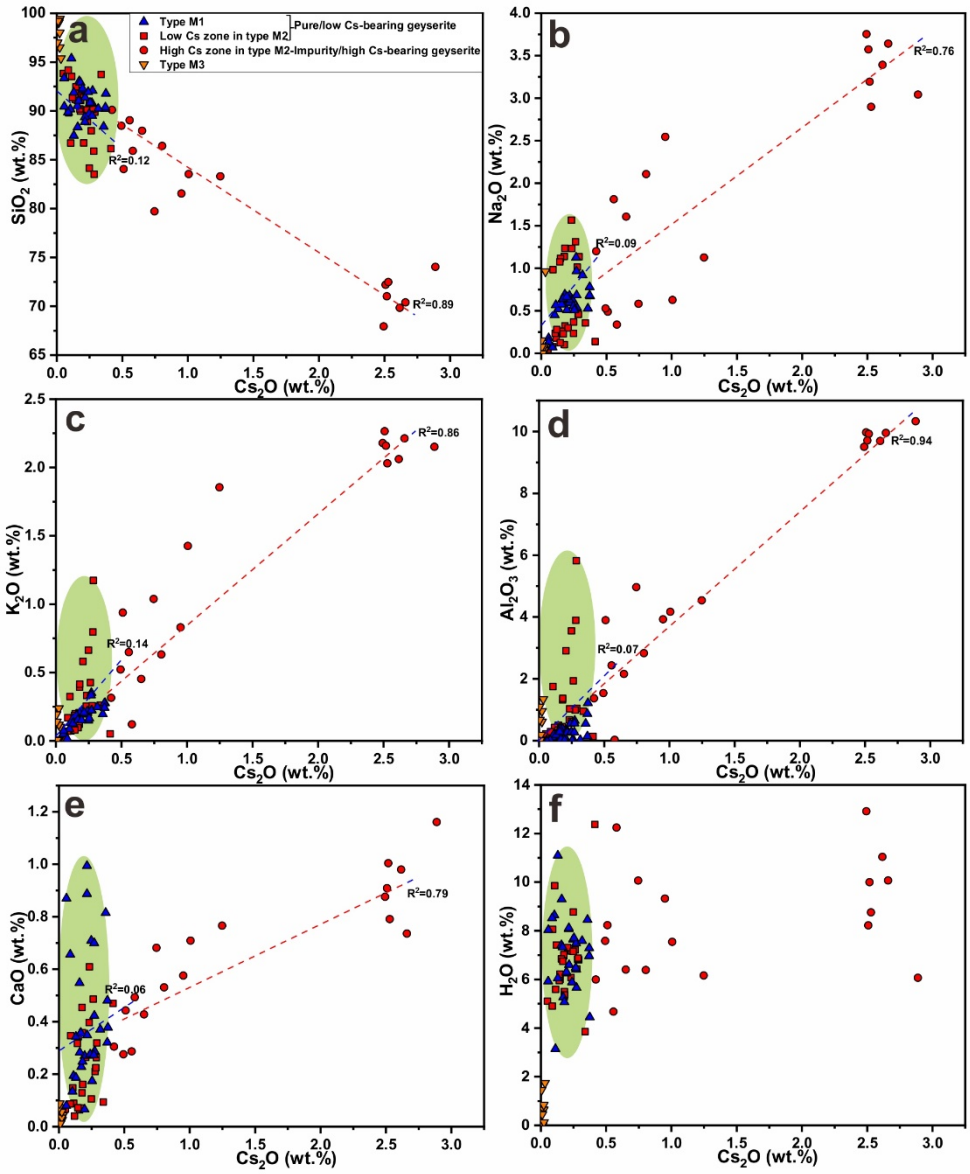

Figure 6. Correlation diagrams between Cs_2O and SiO_2 (a), Na_2O (b), K_2O (c), Al_2O_3 (d), CaO (e), H_2O (f). Blue line represents correlation in low Cs-bearing ore. Red line represents correlation in high Cs zone in high Cs-bearing ore. Light green area denotes the area of low Cs-bearing ore.

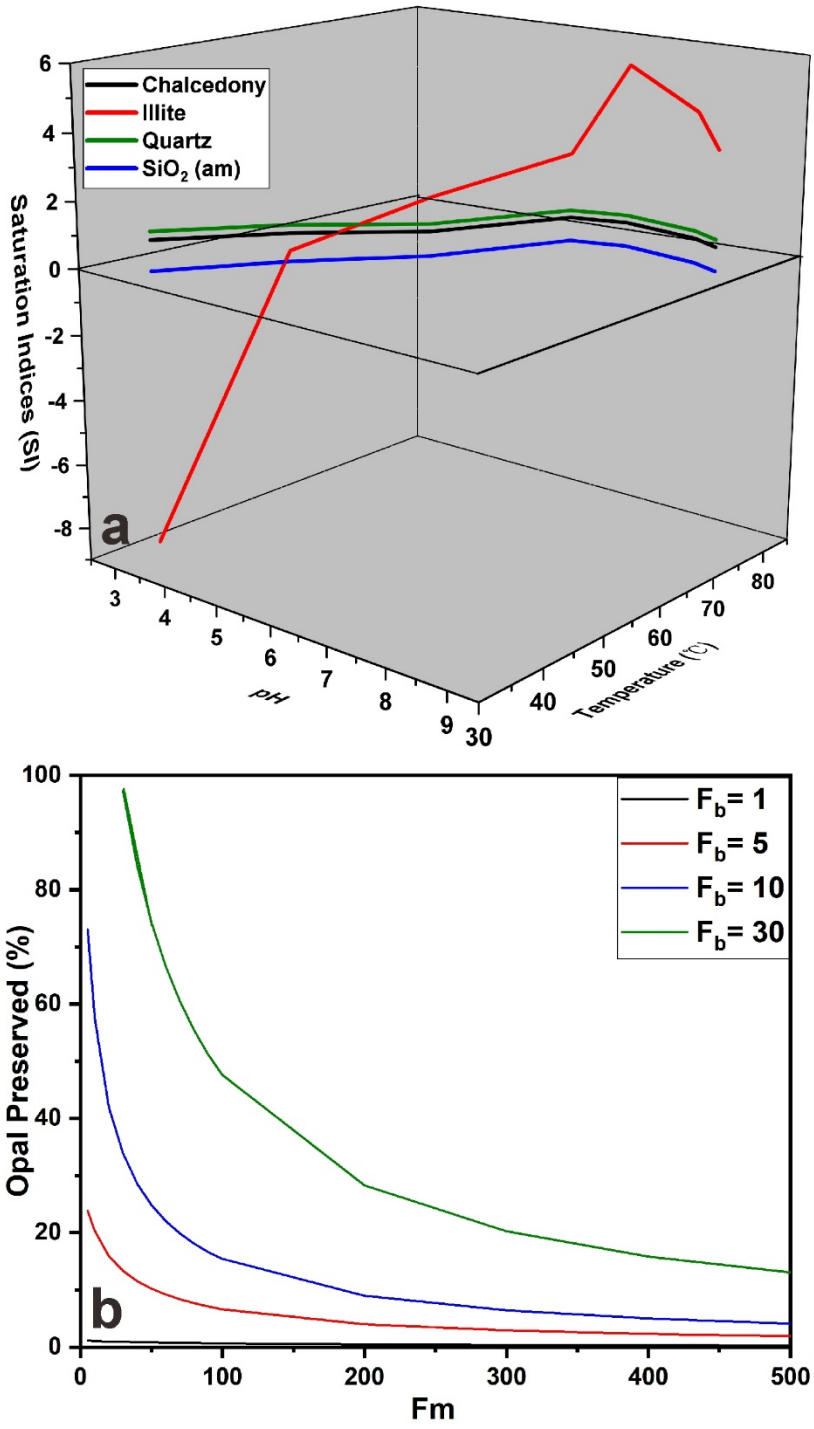

Figure 7. (a) Mineral saturation indices (SI) with different pH and temperature; (b) the relationship between clay input (F_m) and ratio of the rain input and opal input (F_{er}/F_m).

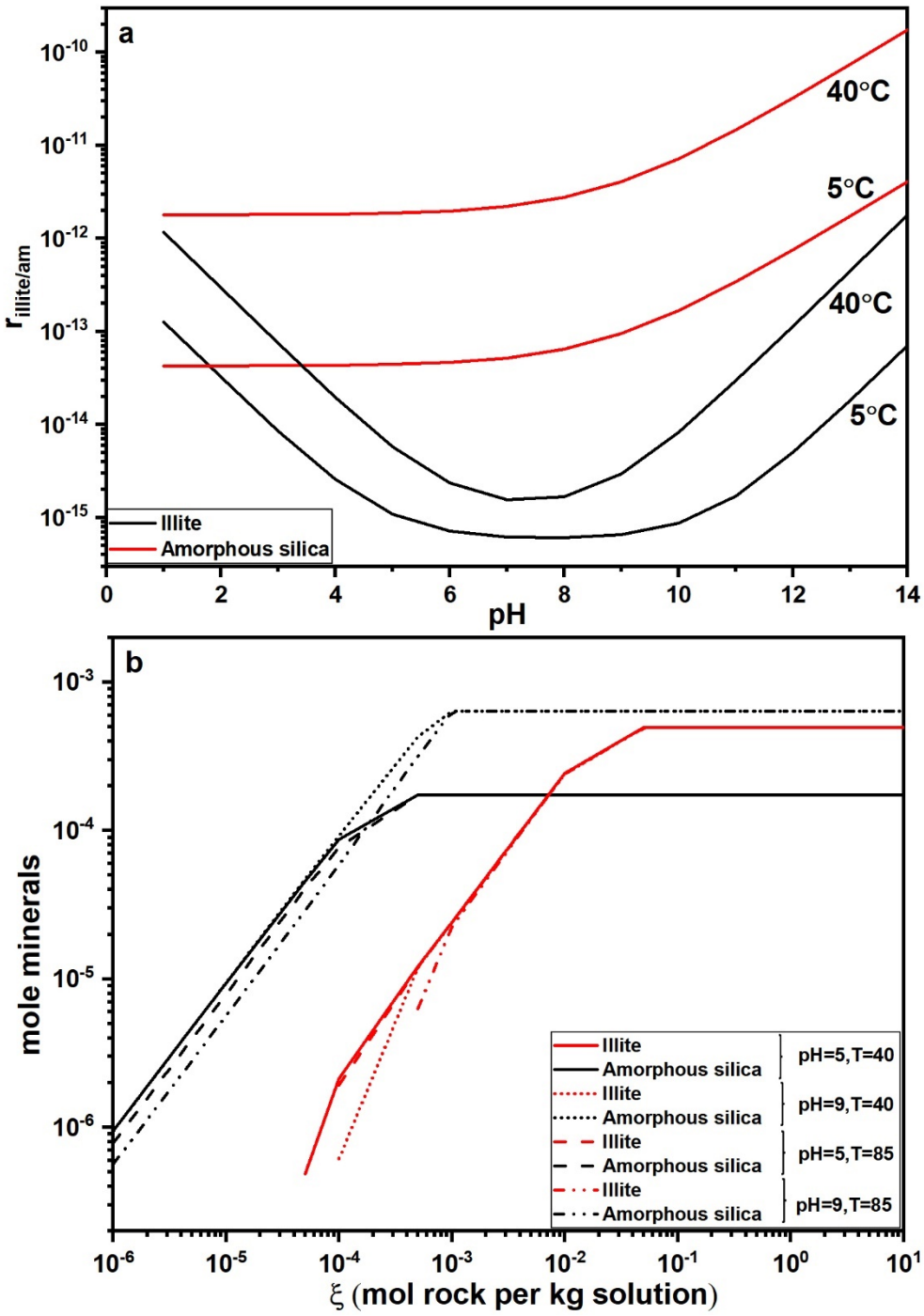

Figure 8. (a) The dissolution rates of amorphous silica and illite at pH of 1-14; (b) mineral formed upon meteoric water-rock interaction.

Table 1. Parameters values applied in the diageneses model.

Parameter	Symbol	Value
Rate constant for opal dissolution	k_s	30 y^{-1}
Saturation concentration of dissolved silica	C_s	$\log C_s = -8.476 - 485.24 \times T^{-1} - 2.268 \times 10^{-6} \times T^2 + 3.068 \times \log T$
Si diffusion coefficient	D_s	100 $cm^2\ y^{-1}$
Intrinsic density of opal	$\rho_{b_{opal}}$	2.1 g cm^{-3}
Intrinsic density of clay	$\rho_{m_{clay}}$	2.6 g cm^{-3}
Porosity	φ	0.8
Input fluxes of opal	F_b	1-30
Input fluxes of clay	F_m	5-500

Table 2. Input values of meteoric water and rock for geochemical meteoric water-rock modelling.

Parameter	Value [a]	Rock parameter	Value
Temperature	5	Temperature	40-85
pH	5	pH	5-9
Major elements (ppm)		Major elements (wt.%) [b]	
SiO_2	0	SiO_2	0.86
Na	15	Al_2O_3	0.028
K^+	18	CaO	0.009
Cl^-	14	Na_2O	0.008
Ca^{2+}	46	K_2O	0.007
Mg^{2+}	3	Fe_2O_3	0.002
SO_4^{2-}	60		
F^-	3		

[a] is physical and chemical condition of meteoric water from Wu et al. (2014). [b] is the average elements composition of ore at stage V from Table A1.